VERIFICATION OF THE THREE DIMENSIONAL SHOCK-STRUCTURES IN AN S-SHAPED TRANSONIC UHBR FAN-ROTOR

L. Meillard - R. Schnell - E. Nicke - M. Voges - C. Voigt

Institute of Propulsion Technology, German Aerospace Center (DLR), Cologne, Germany,
lionel.meillard@dlr.de

ABSTRACT

The German Aerospace Center (DLR) has designed and tested a 1:3 scaled model S-shaped fan rotor as an example for a medium pressure ratio propulsor with potential application to future UHBR aero engines. In the present study, the attention will focus on the tip region in which the flow field is subject to complex flow phenomenona and to the impact of the S-shape feature on the radial shock structure. Steady numerical simulations with DLR in-house solver TRACE as well as measurements were carried out. The casing is instrumented with ten piezoelectric static pressure transducers over the rotor pitch. Particle Image Velocimetry (PIV) is used to catch the flow velocities at three radial blade positions. All experimental data require a phase-locked ensemble averaging procedure. The results include the global performance of the compressor and detailed comparisons between simulations and measurements to validate the shock structures as well as the highly three dimensional-design S-shape fan.

NOMENCLATURE

Abbreviations

ACARE	Advisory Council for Aeronautics Research in Europe	RANS	Reynolds-Averaged Navier-Stokes
		SFC	Specific Fuel Consumption
		SRA	Strategy Research Agenda
BS	Bow Shock	TE	Trailing Edge
CAD	Computer-Aided Design	TLV	Tip Leakage Vortex
CCD	Charge-Coupled Device	TRACE	Turbomachinery Research Aerodynamics Computational Environment
CFD	Computational Fluid Dynamics		
DLR	German Aerospace Center	UHBR	Ultra-High Bypass-Ratio
ISA	International Standard Atmosphere	**Variables**	
LE	Leading Edge	f_s	Sampling Frequency
M2VP	Multistage Two Shaft Compressor Test Facility	mag	Magnitude Velocity
		r	Radial Position
PIV	Particle Image Velocimetry	u	Axial Velocity
PS	Passage Shock	v	Circumferential Velocity

INTRODUCTION

The European Commission's "European Aeronautics: Vision 2020" and the Strategy Research Agenda (SRA) written by the Advisory Council for Aeronautics Research in Europe (ACARE) [1] give the following imperatives "More safer, affordable, cleaner, and quieter". This leads in part to a reduction of 50% of the perceived noise and the emitted CO_2 and 80% of the NO_X emissions. These ambitious goals are not achievable without the development of new technologies and important breakthroughs. In this context, the fan of civil aircraft engines is more and more in the focus of
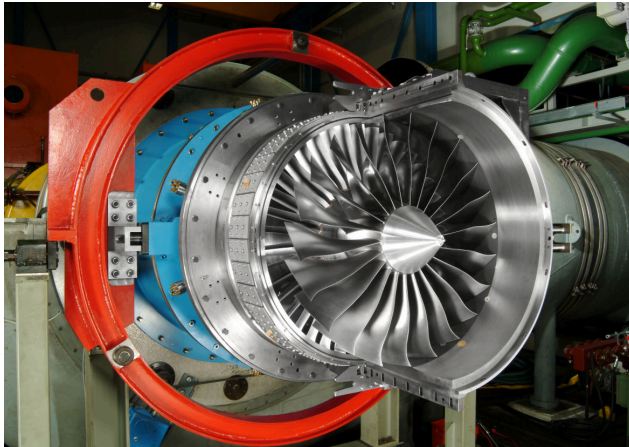
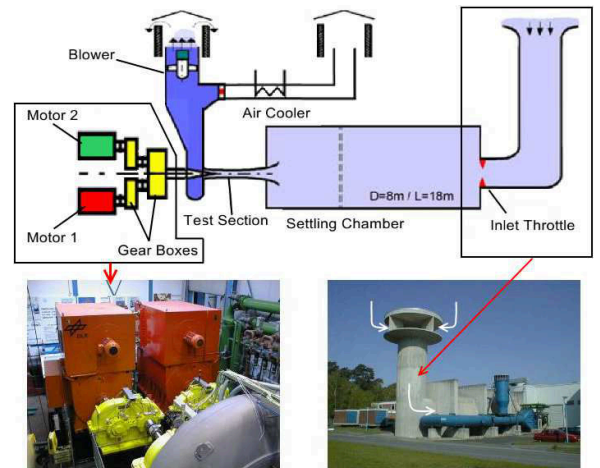Figure 1: **UHBR-Fan located at the Multistage Two Shaft Compressor Test Facility (M2VP) without instrumentations**

Figure 2: **Setup of the Multistage Two Shaft Compressor Test Facility (M2VP)**

research due to the trend to increase the engine´s bypass-ratio as one of the major technological means for reducing the engine´s Specific Fuel Consumption (SFC). One research topic of the DLR Institute of Propulsion Technology is focused more particularly on Ultra-High Bypass-Ratio (UHBR) fans as seen in Figure 1. A test rig representative of a modern high bypass-ratio engine, directly derived from a design study carried out during the European project Silencer, was thus designed and tested. The specific criteria [5, 6, 9] used are summarized as follows:

- A high bypass-ratio of the whole engine over >12 to reduce fuel consumption and to increase the propulsive efficiency of the aircraft.

- A low speed to reduce fan tip noise such as buzz-saw at take-off, and avoid the formation of strong shocks in the rotor tip region.

- An approximately 10 % higher specific flow rate to minimize the fan diameter, thereby the weight can be reduced as well as the nacelle losses.

The use of a S-shaped rotor leading edge results in a best compromise between high efficiency and an increase of the compressor working range. It impacts on the shock structure compared to an unswept rotor have been described in [3, 5]. It was observed that the major difference between them lies in the fact that the S-shaped rotor leads to the formation of double shocks on the suction surface whereas an unswept rotor gives a conventional single shock.

A first measurement campaign was successfully carried out as described in detail [4, 10] providing a general assessment in terms of the fan performance which fully matches with the numerical results as reported in [7]. In this study the investigations have been extended to other specific instrumentations focused on the flow field in the tip gap. This region is still not yet well understood and subject to complex phenomena such as interactions between the tip clearance flow, passage shock and boundary layer inducing strong losses. In order to reach a deeper understanding of this flow, Particle Image Velocimetry (PIV) and end wall static pressure probes at the casing above the rotor are used.

In the present investigation, the results from the steady simulation will be compared with measurements from PIV and end wall unsteady pressure transducers. By this way the quality and the accuracy of the simulations will be assessed. Then the flow will be further analyzed to validate the
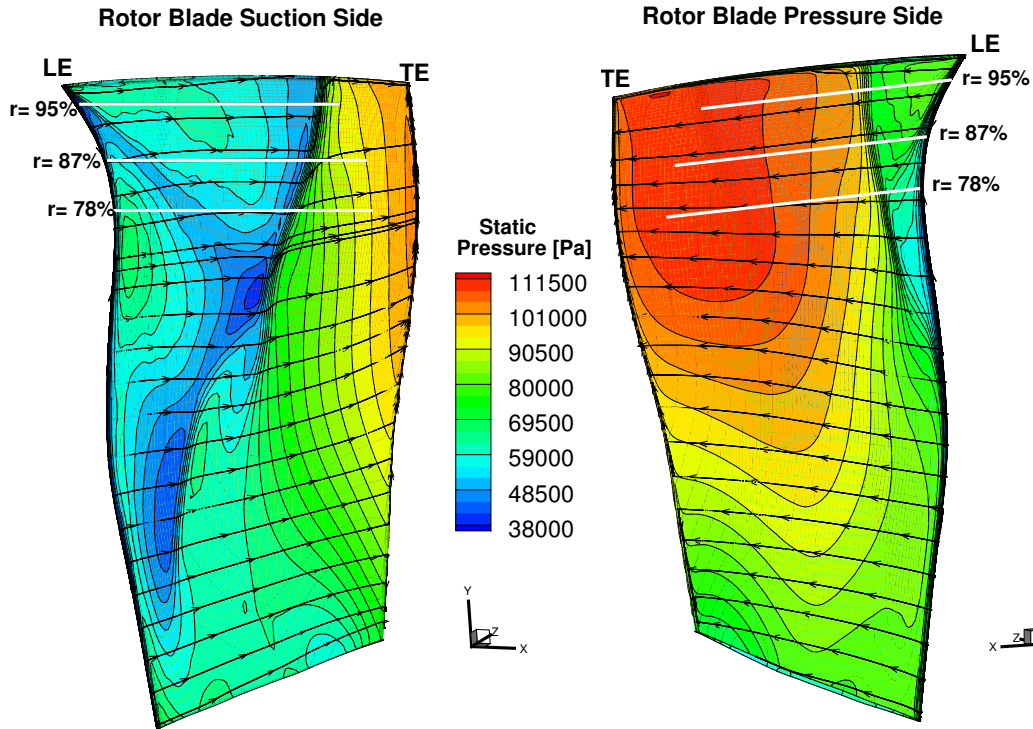
Figure 3: **Static pressure distributions from CFD results on the suction side (left) and on the pressure side (right) near peak efficiency (PT 4) at 100 % nominal speed, and radial positions of the three PIV light sheets**

three dimensional structure of the shocks according to the span-wise direction depicted in Figure 3 in which the static pressure and the streamlines on the blade surfaces at 100 % nominal speed near peak efficiency are represented. The comparison of the two measurement techniques aims at demonstrating the capability of the PIV approach to detect the shocks at the correct position, in this way a confidence is given in the PIV data which were performed deeper in the blade passage and for which no validations could be made via static pressure sensors.

NUMERICAL METHOD

As previously reported by Meillard [7], simulations are carried out using the solver TRACE [2] developed at the DLR Institute of Propulsion Technology. All simulations are achieved by solving the steady-state Reynolds-Averaged Navier-Stokes (RANS) equations in a single blade passage of the actual compressor's geometry. This solver is based on the finite volume method using a second order scheme. Turbulence is modeled by the k-ω Wilcox model.

A computational grid of 4.2 million cells is based on an OCH topology of structured blocks, as can be seen in Figure 4, leading to a mesh of 123 nodes in the blade-to-blade direction, 101 nodes in the span-wise direction and 123 nodes in the stream-wise direction. The boundary layer mesh around the blade wall is a Low-Reynolds mesh.

Total pressure, total temperature and flow angle are defined uniformly at the inlet boundary following the International Standard Atmosphere (ISA) conditions. Viscous-wall and adiabatic conditions are imposed on all solid walls. A boundary layer and pressure profile at the inlet as well as the tip gap are all derived from the measurement data as presented by Schnell [10].
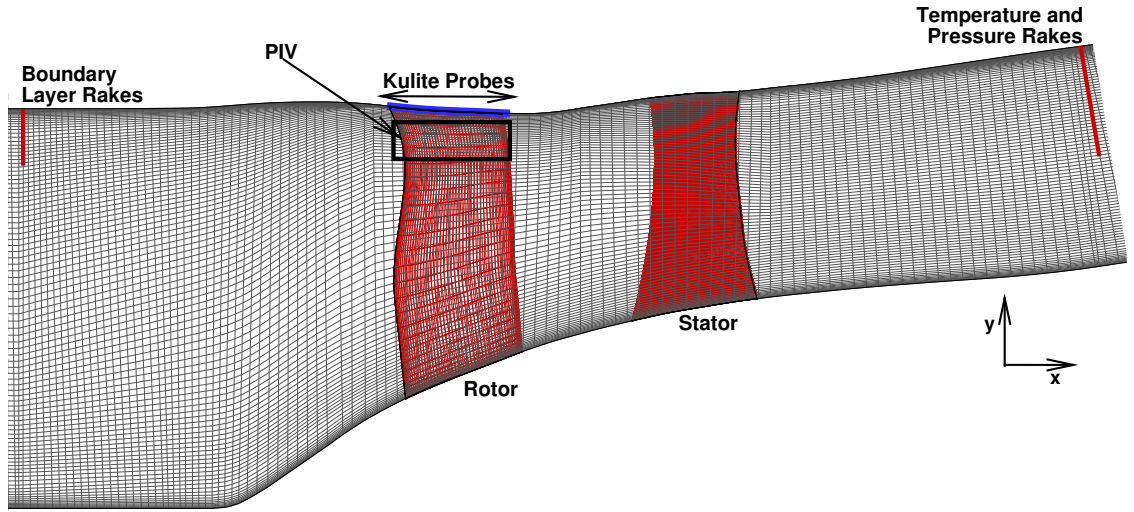
Figure 4: **Zones of investigation by the sensors and computational grid viewed in the meridional plane**

The post-processing of the simulations aimed at comparing the simulation data with the measurement data. Special attention has been paid to the exact location of measurement visualizations and to the studied parameters.

EXPERIMENTAL SETUP
Test Configuration

The UHBR rig under investigation is experimentally tested at the Multistage Two Shaft Compressor Test Facility (M2VP) at the Institute of Propulsion Technology at Cologne. The design of this fan were optimized by DLR to meet aerodynamic and acoustical constraints in order to reduce the noise at take-off and the fuel consumption. The parameters can be found in Table 1. This single stage compressor is composed of 22 rotor blades and 38 stator vanes.

The M2VP test facility, see Figure 2, uses two electric motors, each providing 5 MW, which are coupled by gear boxes to reach a maximum rotational speed of 20,000 RPM. An inlet tower and a settling chamber of 8 m diameter and 18 m length are positioned in front of the test section. The air exits through a blower. An exit throttle help to set the mass flow.

The experiments featured probe and rake measurements upstream of the rotor and downstream of the stator in order to determine global performance of the fan in terms of efficiency and total pressure ratio as seen in Figure 4.

Rotor diameter	0.8 m
Hub to tip ratio	0.275
Shaft speed at design point	7846 1/min
Blade tip speed	330 m/s
Relative Mach number at blade tip	1.05

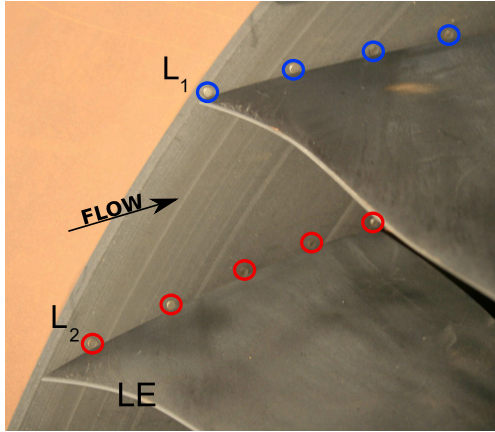Table 1: **Design parameters of the UHBR fan**

Figure 5: **Static pressure sensors and blade locations seen from the inside of the UHBR rig (in blue probes belonging to L_1, in red probes belonging to L_2)**
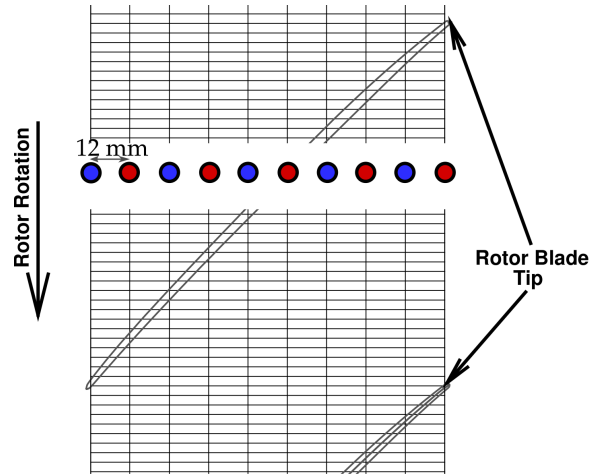

Figure 6: **Spatial resolution of wall pressure measurement after probe synchronization (in blue probes belonging to L_1, in red probes belonging to L_2)**

Static Pressure Measurements

The clearance gap region was investigated by ten axial piezoelectric static pressure transducers placed at the casing above the rotor, see Figure 5, providing a sensitivity of about 35 Pa in a pressure range of 3.5 bar. Two arrays, L_1 and L_2, of five sensors each, are shown in Figure 5. They are circled in blue and red respectively. The distance between the two arrays is one blade pitch. This specific arrangement avoids manufacturing problems, for example weaknesses inside the casing structure and space limitation. The distance between two consecutive sensors (one from L_1 and one from L_2) in the axial direction is 12 mm and defines the spatial resolution of wall pressure measurement as seen in Figure 6.

The raw signal from the unsteady pressure measurement transducers is processed in order to compare it with the simulation data. The signals are triggered by the rotor revolution, registered by a sampling frequency f_s and then converted by a 24 bit converter. A re-sampling procedure leads to a resolution of 38 points per blade pitch.

Because of the arrangement in two arrays, time synchronization is performed to bring all the probes into phase with each other as seen in Figure 6. The phase-lock averaging method suppresses stochastic fluctuations in the raw time series signal to make it comparable with the steady simulations. The phase average is achieved from more than 400 rotor revolutions. It has been demonstrated in [7] that above this number of revolutions no significant effects are visible in the averaged signal. Finally, to meet ISA conditions in the numerical set up, the static pressure is normalized by the reference pressure P_{ref} in the settling chamber.

Velocity Measurements

The Particle Image Velocimetry (PIV) allows measuring the flow velocity in a confined space offering high spatial resolution. The reliability of this technique under transonic conditions as well as all the details concerning the PIV setups are given by Voges [11, 12].

The rig has been modified by installing a transparent window in order to receive the PIV instrumentation, see Figure 7. The PIV setup deflects the laser beam into planes in the compressor with the help of one probe. This probe is traversed to adjust the laser light sheet at three radial blade heights giving the topmost light sheet at 95 % blade height, the second one at 87 % blade height and the lowest
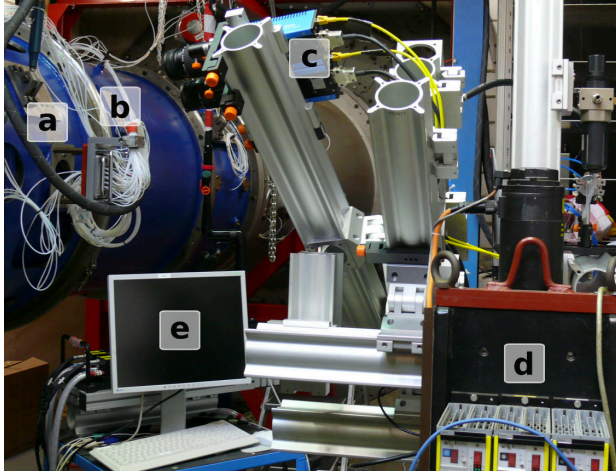
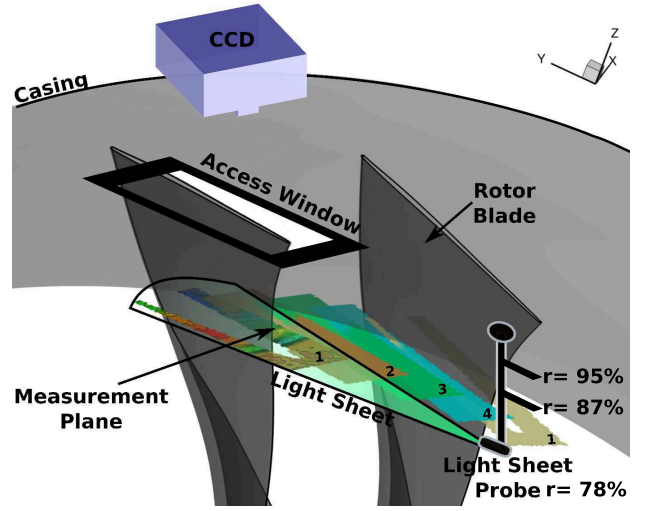Figure 7: **PIV setup: (a) Rig, (b) Optical access, (c) CCD camera, (d) Laser sources, (e) Data acquisition**

Figure 8: **Schematic setup of the PIV measurement and of the four light sheets measurements in the blade channel at r= 78 %**

one at 78 % blade height.The plane positions are depicted in the CAD model in Figure 8.

This technique requires particles to highlight the trajectory of the flow illuminated by the beam, therefore oil droplets of 300 nm to 800 nm size are injected at the axial center of the settling chamber. In this way a homogeneous particle distribution within the compressor is ensured and provides an adequate resolution to characterize strong shock waves [12].

The flow is visualized with CCD (Charge-Coupled Device) camera seen in Figure 7 c with 1600×1200 pixels resolution providing a magnification factor of 15 px/mm and operating at 5 Hz frame rate. Calibration is used because of the optical effect of the inner cylindrical surface observation at the casing inducing a deformation of the visualizations. Phase constant PIV measurement is triggered by the rotor blade permitting to divide one blade passage into four constant phase angles (as seen in Figure 8 where plane one is repeated two times to complete a whole pitch) for which phase-lock averaging is used over at least 400 images.

Concerning the post-processing, the blade passage measurement has been reconstructed for each of the three radial light sheet positions by adding the five successive measurement planes, as seen in Figure 8, into a single plot. The same method has been achieved for the simulation in order to make accurate comparison with the measurement data. In this way, the same simulation regions are investigated. It should be noted, that all the simulation planes have been deliberately created longer in the x direction than allowed by the flow field of the camera view, in such a way more information concerning the flow structure upstream can be obtained from CFD calculations. The reconstructed flow field in the pitch direction leads to visible discontinuities at the interface between two consecutive surfaces. That can be explained by the fact that the end of one plane is not located at the same radial position than the beginning of the next plane. The color contours represent the magnitude or circumferential absolute velocities which have been projected onto each plane. Because the radial velocity is missing in the measurement data, the magnitude velocity is defined for calculations as well as for measurements by equation 1 in which u and v represent the axial and the circumferential velocities respectively.

$$mag = \sqrt{(u^2 + v^2)} \qquad (1)$$

SELECTED OPERATIONS CONDITIONS

The measurement program has been focused on the investigation of 100 % nominal rotor speed being representative for the maximum climb in flight condition. The measurement points and the speed line analyzed are displayed in Figure 9. Circumferential velocity from PIV measurement matches to colored triangles (MP 13, MP 21 and MP 27) and static pressure matches to the black one (MP 11).

It should be mentioned here that the same operating points cannot be reproduced in particularly for the PIV measurements. As it was explained above, this technique needs to stop the data acquisition in order to modify the light sheet positions inducing a non-reproducibility of the operating points. It is assumed that even though the three light sheets were performed sequentially and that the operating points were not perfectly reproducible for each three light sheets, the set of velocity data is still consistent due to the phase averaging technique making the fluid structures traceable through the different planes [11, 12].

For the comparison between measurement and simulation, an operating point PT 9 near peak efficiency from the simulation is compared to the set of measurement operating points.
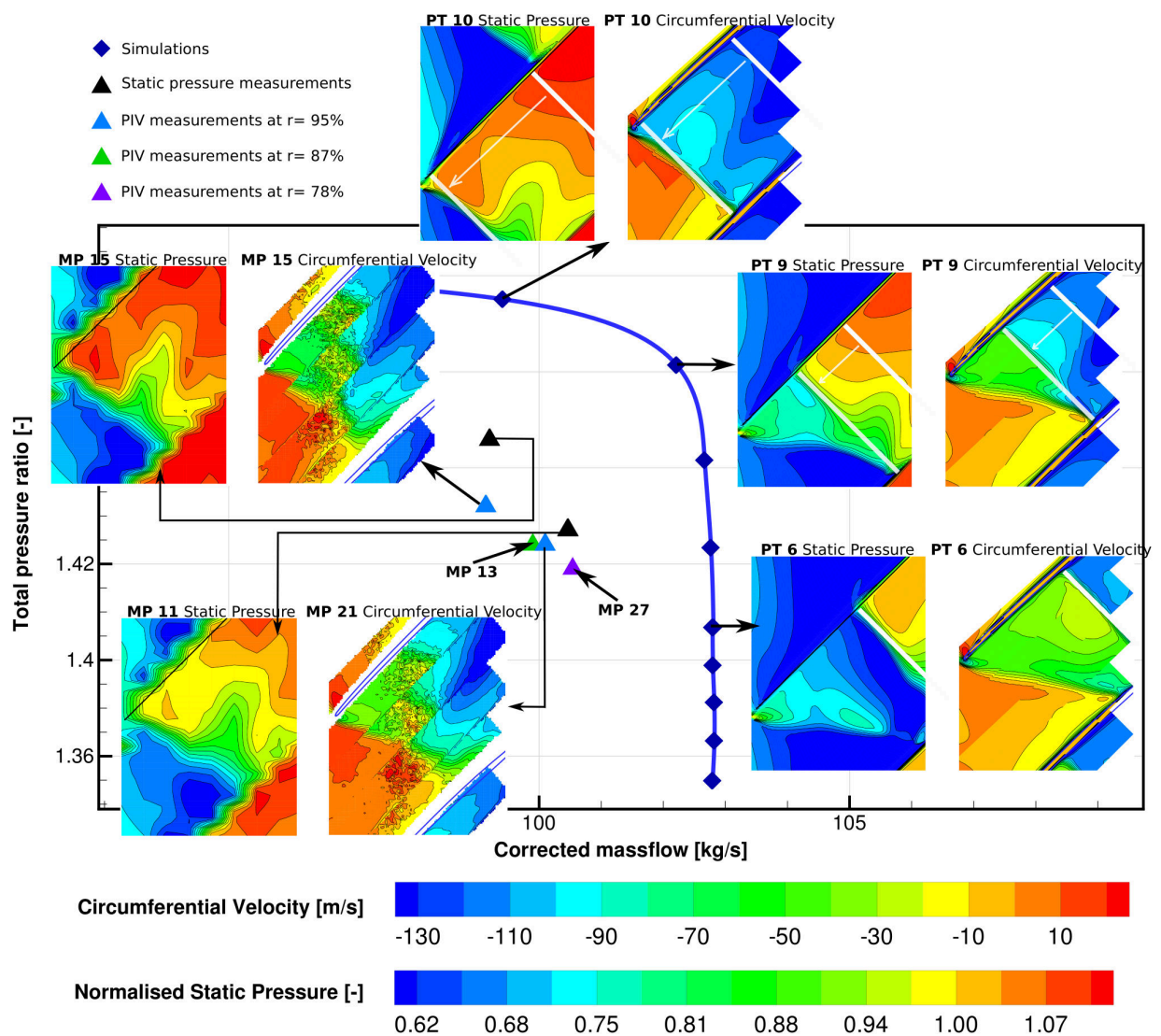

Figure 9: **Sensitivity of the static pressure at the casing and circumferential velocity at r= 95 % regarding the corrected mass flow**

RESULTS

Sensitivity

In Figure 9 examples of measured static pressure at the casing and contour plots of circumferential velocity at r= 95 % contour plots are given along the 100 % speed line in transonic condition for the simulations (PT #) as well as of the measurements (MP #). On all the contour plots, the direction of the fan revolution is from up to down as indicated in Figure 6.

Similar flow structures and its evolutions are visible in Figure 9 for calculations and measurements. The level of the pressure increases with the total pressure ratio whereas the corrected mass flow decreases. Moreover for circumferential velocity and static pressure, the passage shock is perpendicular to the blade chord by connecting the pressure side of one blade to the suction side of the next one. The shock position moves upstream when the corrected mass flow decreases as highlighted by the arrows until the leading edge is reached as depicted for PT 10 operating point.

The bow shock is still attached to the leading edge for the operating conditions PT 6 to PT 10 of the numerical data as well as for the measurement data. The set of points representing the measurement data MP 11, MP 15, and MP 21 show a passage shock already merged with the bow shock. That is coherent because the ranges of the MP's corrected mass flow are close to the value of the PT 10 corrected mass flow of about 99 kg/s for which the passage shock and bow shock are merged, making the bow shock shape perpendicular to the blade channel.

Moreover, interactions between tip leakage vortex and shock are observed on the static pressure plots. They are characterized by a low pressure appendix located downstream the passage shock, giving in this way an idea of the tip leakage trajectory. It should be noticed that no interactions are visible on the CFD velocity data whereas discrepancies are located on the measurement data plots. Those discrepancies could be caused by a high concentration of tracking particles with a low velocity.

Comparisons and validations

In Figure 10 a cross comparison between simulation and measurement techniques (static pressure and PIV) is depicted. The two rows give respectively the circumferential velocities at r= 95 % and the static pressure at the casing. The investigated regions are not located exactly at the same radial positions depending of the measurement techniques used in the tip region. The simulations show the passage shock with a high gradient whereas the measurement data present the extension of the passage shock larger in the blade channel direction as it was already observed by Meillard [7]. A twin shocks structure is well visible on the simulation whereas the PIV and transducer techniques reveal a unique shock. Indeed, that is due to the fact that the measurement points MP 11 and MP 21 have a higher backpressure inducing an upstream displacement of the passage shock. By comparing the two measurement techniques a same flow topology is observed: passage and bow shocks are merged and attached to the leading edge joining the two blade surfaces. Additionally, the discrepancies located in the circumferential velocity plot form a similar tip leakage trajectory on the static pressure. It should be noticed that the interaction between flow and shock system is not obvious on the PIV measurement. A confidence is now given to the PIV data for further investigation deeper in the blade span.

In Figures 11 and 12 the simulation results (left) of three radial light sheet planes ,combined in three dimensional views, are compared to the measurement data (right). Here, the figures are split into three views for each radial position in order to make the comparison easier. The blade surface, on which the calculated static pressure has been displayed, is also depicted in all figures to give a reference position to the structure of the phenomenon occurring pitch-wise on the blade. For reasons of readability and clarity, only one part of the static pressure on the blade is represented to keep the blade channel visible. Attention has been paid on the fact that the direct vicinity of the blade has not been caught by the PIV measurement due to reflective effect of the blade surface. For this reason
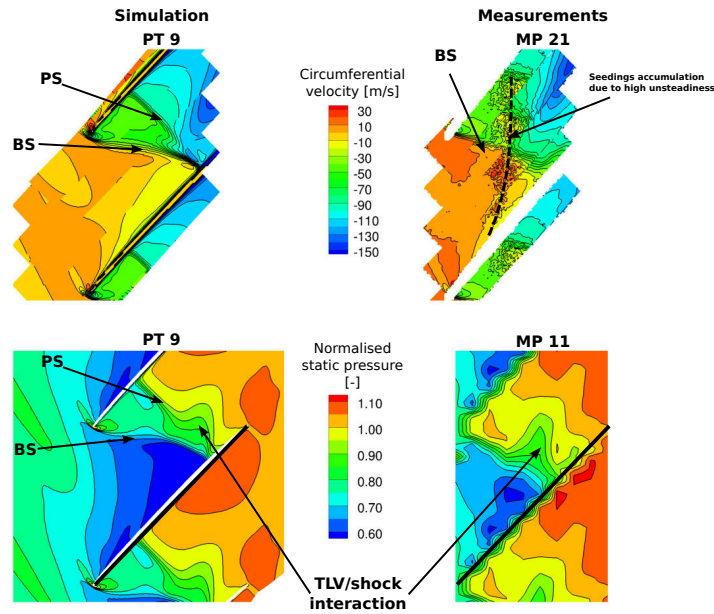
Figure 10: **Validation of the calculated shock structure via cross checks between PIV measurement techniques at r= 95 % and with static pressure [8]**

the blade profile on the measurement data seems to be larger and longer than the blade geometry in the circumferential view. This combination of the three light sheets displays the three dimensional structure of the shocks and its evolutions along the radial position.

The flow coming from the inlet in Figure 11 is homogeneous near the blade tip at r= 95 % with a magnitude of about 130 m/s. This is not the case for the two other radial positions because the presence of a bow shock cross the inlet region inducing a discontinuity of the flow. Then the magnitude velocities for the calculated and the measurement data increase gradually by approaching the leading edge until the passage shock is reached. This acceleration is more pronounced for the simulation and it occupies all the pitch. The flow field structure between the leading edge and 25 % blade chord length is not in good agreement for the magnitude velocity and is again worse for the upper radius planes with the presence of the reflective problem expanding on all the pitch-wise direction at about 40 % blade chord. Then behind the passage shock the velocity flow field is lower and fits better for all the figures. But a relatively good agreement can be observed in terms of magnitude velocity levels in Figure 11 for all radial positions.

As already explained, the shock locations are put into evidence with the circumferential velocity contour plot in Figure 12. This one offers again an enhancement of the shock position determination even though the passage shock is not clearly defined on the measurement data. CFD circumferential velocity levels are lower than the measurement ones especially in the inlet region as observed in Figure 12. For all the radial positions the bow shock is attached to the leading edge, that is in agreement with the operating condition. Simulation and measurement show the same tendency concerning the bow shock slope within the blade channel. At higher span positions, the bow shock is approximately axial leaving the leading edge until the second half part of the passage width and then it turns to be perpendicular at the suction side of the neighbouring blade. At lower positions, the angles formed by the bow shock and blade chord at the leading edge become more and more perpendicular when the radius decreases. Moreover, the simulations prove that the passage shock travels upstream when the radius decreases until it is very close to the bow shock. The calculated shock structures are well visible for all radial position.
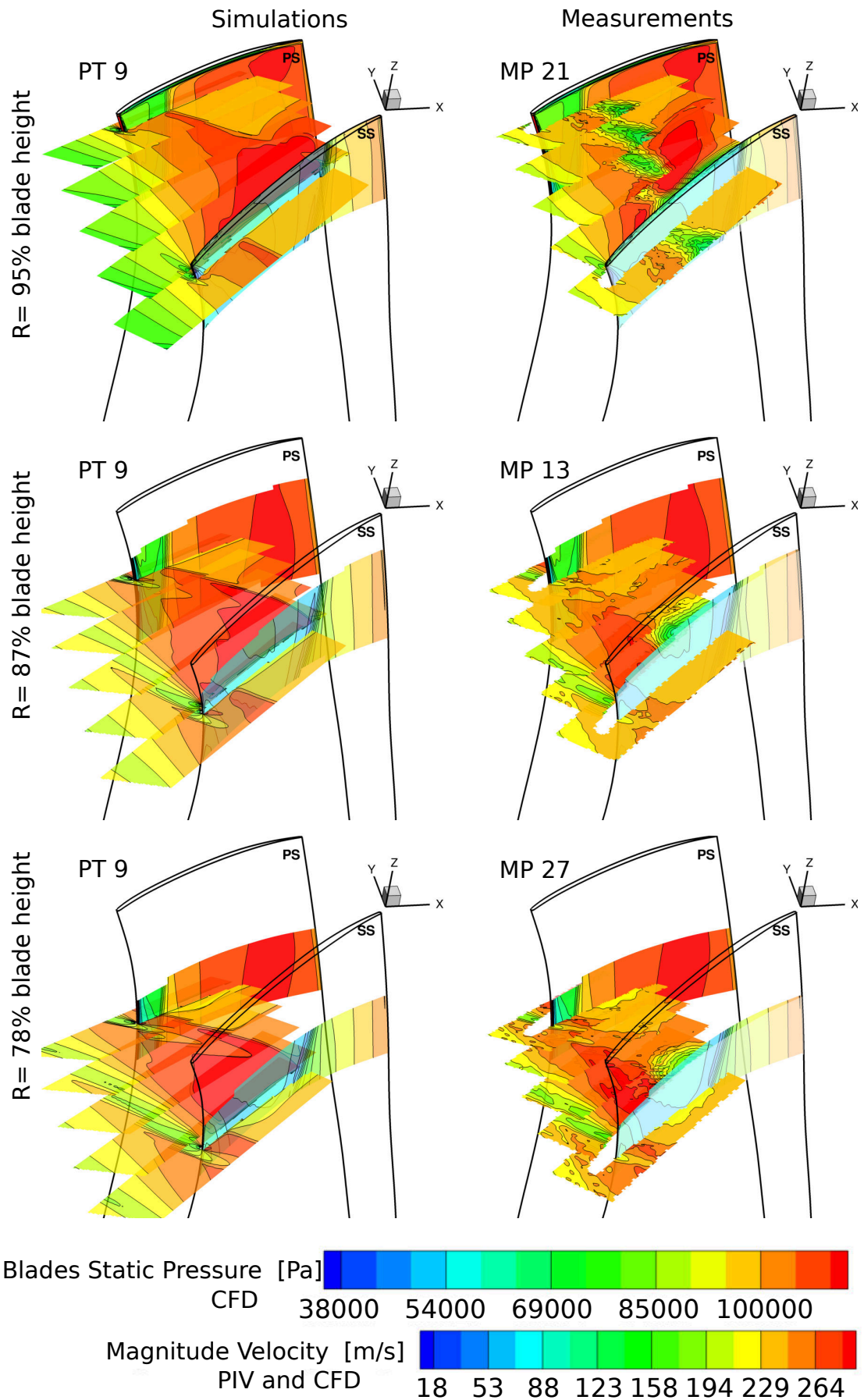
Figure 11: **Magnitude velocity at three different blade height positions and blades´ static pressure, inlet is left**
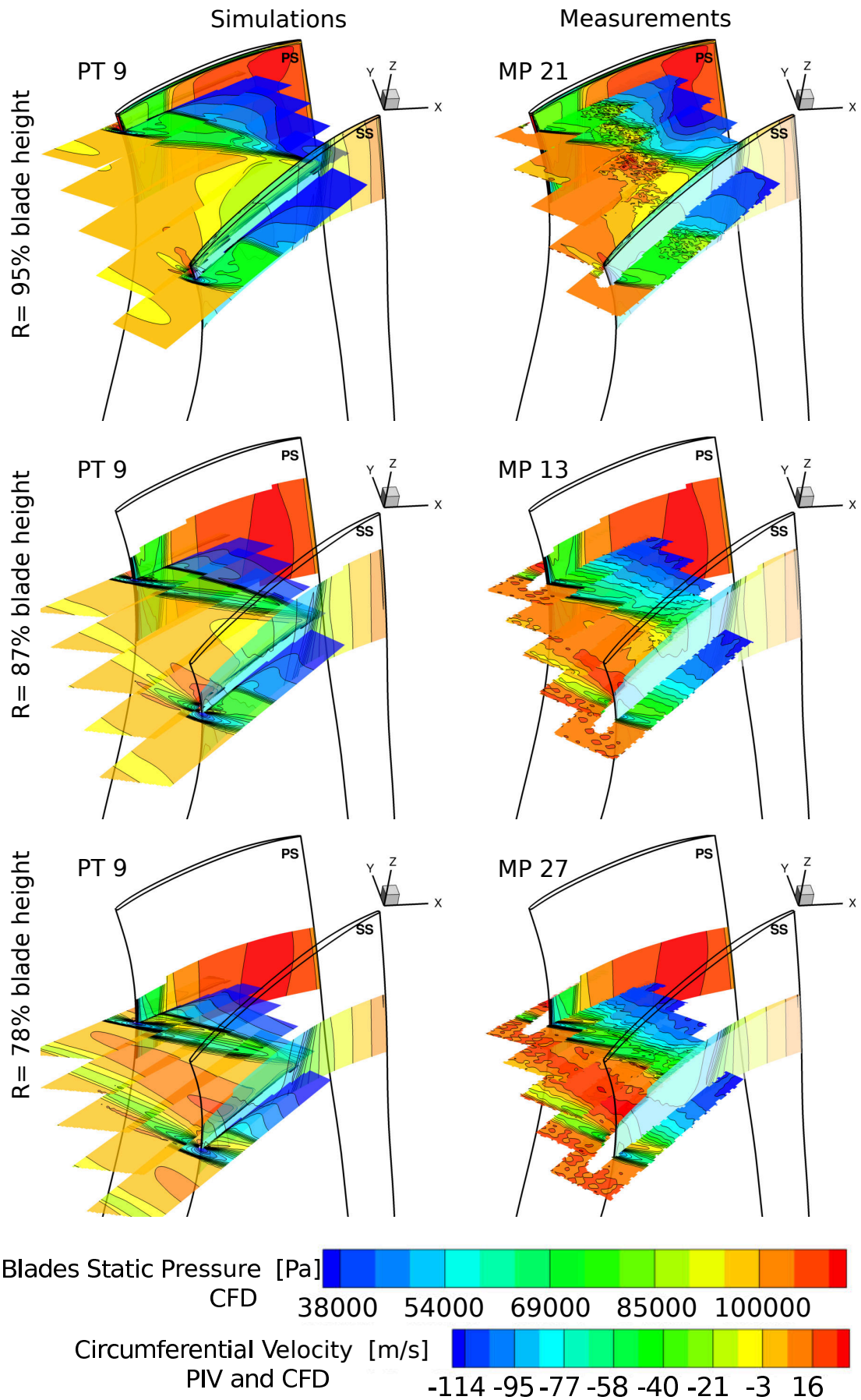
Figure 12: **Circumferential velocity at three different blade height positions and blades´ static pressure, inlet is left**

CONCLUSION

In the present study, the complete blade tip channel region has been investigated by the ten pressure transducers whereas only one part of the rotor inlet and one part of the blade airfoil can be visualized with the PIV instrumentations due to limited optical access. However, PIV measurements provide more information of the flow field at three different radial positions inside the blade passage.

The circumferential velocity has been chosen because it has the advantage to show the shock positions. PIV technique measurements at r= 95 % blade height have been cross checked with simulations and static pressure data coming from the transducers. Its capability to catch shock positions in transonic flow conditions is proved. A quite good agreement was observed for the bow shock position whereas the passage shocks were not visible due to the operating point chosen.

Then a reconstruction of the shape and the structure of the compression shock waves have been analyzed in the span-wise direction at three different blade radial positions. Good agreement has been observed in terms of the velocity level. The three dimensional bow shock structures are well represented in the numerical data in terms of positions and gradients. For all investigated points, this shock is attached to the leading edge. Moreover, the simulation data show that the passage shock is further downstream in the tip region of the S-shape blade permitting a better stall margin.

References

[1] P. Arguelles, M. Bischoff, P. Busquin, B. Droste, R. Evans, W. Kroll, JL Lagardere, A. Lina, J. Lumsden, D. Ranque, et al. European aeronautics: A vision for 2020. *Report of the Group of Personalities, The European Commission*, 12, 2001.

[2] K. Becker, K. Heitkamp, and E. Kügeler. Recent progress in a hybrid-grid CFD solver for turbomachinery flows. *V European Conference on Computational Fluid Dynamics, Lisbon, Portugal*, June 2010.

[3] J.D. Denton. The effects of lean and sweep on transonic fan performance: a computational study. *Task Quarterly*, 6(1):7–23, 2002.

[4] A. Giebmanns. Experimentelle und numerische untersuchungen des aerodynamischen verhaltens am UHBR-Rig. Master's thesis, Propulsion of Technology DLR, 2011.

[5] B. Kaplan. *Design and experiments of an advanced fan stage with Ultra-High Bypass Ratio*. PhD thesis, Institute of Propulsion Technology DLR, 2009.

[6] B. Kaplan, E. Nicke, and C. Voss. *Design of a Highly Efficient Low-Noise Fan for Ultra-High Bypass Engines*. ASME-paper GT2006-90363, 2006.

[7] L. Meillard. Analyse of the aerodynamic performance of the DLR UHBR-Fan stage: Comparison of detailed experimental data with numerical simulations. Master's thesis, ENSIAME - École Nationale Supérieure d'Ingénieurs en Informatique Automatique Mécanique Énergétique Électronique de Valenciennes, Institute of Propulsion Technology DLR, 2012.

[8] L. Meillard, R. Schnell, R. Meyer, and C Voigt. Time resolved pressure and velocity measurements at the dlr uhbr-fan and comparison with simulation data. *DGLR - 62. Deutscher Luft- und Raumfahrtkongress, Stuttgart*, September 2013.

[9] E. Nicke, V. Plevnik, T. Dabrock, and M. Bunde. Design and build of the DLR UHBR-Fan rig as well as first measurement results. Institute of Propulsion Technology, DLR Cologne, 2008.

[10] R. Schnell, A. Giebmanns, E. Nicke, and T. Dabrock. Aerodynamic analysis of a fan for future ultra-high bypass ratio aeroengines. *ISABE Paper, 19th ISABE Conference Montreal/Canada 2009*, ISABE-2009-1149:10, 2009.

[11] M. Voges, M. Müller, C. Zscherp, R. Schnell, C. Willert, and R. Mönig. Investigation of blade tip interaction with casing treatment in a transonic compressor Part I: Particle image velocimetry. *Journal of Turbomachinery*, 133(1):011007, 2011.

[12] M. Voges, C. Willert, R. Mönig, M. Müller, and H-P. Schiffer. The challenge of stereo piv measurements in the tip gap of a transonic compressor rotor with casing treatment. *Experiments in fluids*, 52(3):581–590, 2012.